

PyFR: An Open Source Framework for Solving Advection-Diffusion Type Problems on Streaming Architectures using the Flux Reconstruction Approach

F. D. Witherden*, A. M. Farrington, P. E. Vincent

Department of Aeronautics, Imperial College London, SW7 2AZ

March 20, 2022

Abstract

High-order numerical methods for unstructured grids combine the superior accuracy of high-order spectral or finite difference methods with the geometric flexibility of low-order finite volume or finite element schemes. The Flux Reconstruction (FR) approach unifies various high-order schemes for unstructured grids within a single framework. Additionally, the FR approach exhibits a significant degree of element locality, and is thus able to run efficiently on modern streaming architectures, such as Graphical Processing Units (GPUs). The aforementioned properties of FR mean it offers a promising route to performing affordable, and hence industrially relevant, scale-resolving simulations of hitherto intractable unsteady flows within the vicinity of real-world engineering geometries. In this paper we present PyFR, an open-source Python based framework for solving advection-diffusion type problems on streaming architectures using the FR approach. The framework is designed to solve a range of governing systems on mixed unstructured grids containing various element types. It is also designed to target a range of hardware platforms via use of a custom domain specific language. The current release of PyFR is able to solve the compressible Euler and Navier-Stokes equations on grids of quadrilateral and triangular elements in two dimensions, and hexahedral elements in three dimensions, targeting clusters of CPUs, and NVIDIA GPUs. Results are presented for various benchmark flow problems, and scalability of the code is demonstrated on up to 104 NVIDIA M2090 GPUs.

*Corresponding author; e-mail freddie.witherden08@imperial.ac.uk.

Program Description

Authors F. D. Witherden, A. M. Farrington, P. E. Vincent

Program title PyFR version 0.1.0

Licensing provisions New style BSD license

Programming language Python, CUDA and C

Computer Variable, up to and including GPU clusters

Operating system Recent version of Linux/UNIX

RAM Variable, from hundreds of megabytes to gigabytes

Number of processors used Variable, code is multi-GPU and multi-CPU aware through a combination of MPI and OpenMP

External routines/libraries Python 2.7, numpy, PyCUDA, mpi4py, SymPy, Mako

Nature of problem Compressible Euler and Navier-Stokes equations of fluid dynamics; potential for any advection-diffusion type problem.

Solution method High-order flux reconstruction approach suitable for curved, mixed, unstructured grids.

Unusual features Code makes extensive use of symbolic manipulation and runtime code generation through a domain specific language.

Running time Many small problems can be solved on a recent workstation in minutes to hours.

Nomenclature

Throughout we adopt a convention in which dummy indicies on the right hand side of an expression are summed. For example $C_{ijk} = A_{ijl}B_{ilk} \equiv \sum_l A_{ijl}B_{ilk}$ where the limits are implied from the surrounding context. All indicies are assumed to be zero-based.

Functions.

δ_{ij} Kronecker delta
 $\det \mathbf{A}$ Matrix determinant
 $\dim \mathbf{A}$ Matrix dimensions

n Element number
 α Field variable number
 i, j, k Summation indices
 ρ, σ, ν Summation indices

Indices.

e Element type

Domains.

Ω Solution domain

Ω_e	All elements in Ω of type e
$\hat{\Omega}_e$	A <i>standard</i> element of type e
$\partial\hat{\Omega}_e$	Boundary of $\hat{\Omega}_e$
Ω_{en}	Element n of type e in Ω
$ \Omega_e $	Number of elements of type e

Expansions.

\wp	Polynomial order
N_D	Number of spatial dimensions
N_V	Number of field variables
ℓ_{ep}	Nodal basis polynomial ρ for element type e
x, y, z	Physical coordinates
$\tilde{x}, \tilde{y}, \tilde{z}$	Transformed coordinates
\mathcal{M}_{en}	Transformed to physical mapping

Adornments and suffixes.

$\tilde{\square}$	A quantity in transformed space
$\hat{\square}$	A vector quantity of unit magnitude
\square^T	Transpose
$\square^{(u)}$	A quantity at a solution point
$\square^{(f)}$	A quantity at a flux point
$\square^{(f_\perp)}$	A normal quantity at a flux point

Operators.

\mathfrak{C}_α	Common solution at an interface
\mathfrak{F}_α	Common normal flux at an interface

1 Introduction

There is an increasing desire amongst industrial practitioners of computational fluid dynamics (CFD) to undertake high-fidelity scale-resolving simulations of transient compressible flows within the vicinity of complex geometries. For example, to improve the design of next generation unmanned aerial vehicles (UAVs), there exists a need to perform simulations—at Reynolds numbers 10^4 – 10^7 and Mach numbers $M \sim 0.1$ – 1.0 —of highly separated flow over deployed spoilers/air-brakes; separated flow within serpentine intake ducts; acoustic loading in weapons bays; and flow over entire UAV configurations at off-design conditions. Unfortunately, current generation industry-standard CFD software based on first- or second-order accurate Reynolds Averaged Navier-Stokes (RANS) approaches is not well suited to performing such simulations. Henceforth, there has been significant interest in the potential of high-order accurate methods for unstructured mixed grids, and whether they can offer an efficient route to performing scale-resolving simulations within the vicinity of complex geometries. Popular examples of high-order schemes for unstructured mixed grids include the discontinuous Galerkin (DG) method, first introduced by Reed and Hill [4], and the spectral difference (SD) methods originally proposed under the moniker ‘staggered-grid Chebyshev multidomain methods’ by Kopriva and Kalias in 1996 [5] and later popularised by Sun et al. [6]. In 2007 Huynh proposed the flux reconstruction (FR) approach [7]; a unifying framework for high-order schemes for unstructured grids that incorporates both the nodal DG schemes of [8] and, at least for a linear flux function, any SD scheme. In addition to offering high-order accuracy on unstructured mixed grids, FR scheme are also compact in space, and thus when combined with explicit time marching offer a significant degree of element locality. As such, explicit high-order FR schemes are

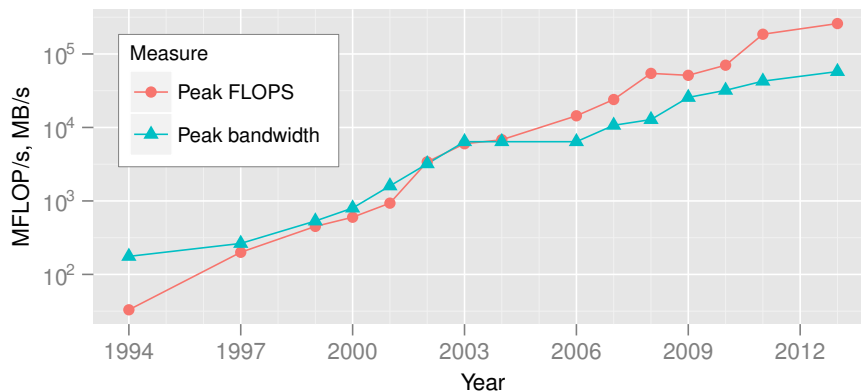


Figure 1. Trends in the peak floating point performance (double precision) and memory bandwidth of sever-class Intel processors from 1994–2013. The quotient of these two measures yields the FLOPS-per-byte of a processor. Data courtesy of Jan Treibig.

characterised by a large degree of structured computation.

Over the past two decades improvements in the arithmetic capabilities of processors have significantly outpaced advances in random access memory. Algorithms which have traditionally been compute bound—such as dense matrix-vector products—are now limited instead by the bandwidth to/from memory. This is epitomised in Figure 1. Whereas the processors of two decades ago had FLOPS-per-byte of ~ 0.2 more recent chips have ratios upwards of ~ 4 . This disparity is not limited to just conventional CPUs. Massively parallel accelerators and co-processors such as the NVIDIA K20X and Intel Xeon Phi 5110P have ratios of 5.24 and 3.16, respectively.

A concomitant of this disparity is that modern hardware architectures are highly dependent on a combination of high speed caches and/or shared memory to maintain throughput. However, for an algorithm to utilise these efficiently its memory access pattern must exhibit a degree of either spatial or temporal locality. To a first-order approximation the spatial locality of a method is inversely proportional to the amount of memory indirection. On an unstructured grid indirection arises whenever there is coupling between elements. This is potentially a problem for discretisations whose stencil is not compact. Coupling also arises in the context of implicit time stepping schemes. Implementations are therefore very often bound by memory bandwidth. As a secondary trend we note that the manner in which FLOPS are realised has also changed. In the early 1990s commodity CPUs were predominantly scalar with a single core of execution. However in 2013 processors with eight or more cores are not uncommon. Moreover, the cores on modern processors almost always contain vector processing units. Vector lengths up to 256-bits, which permit up to four double precision values to be operated on at once, are not uncommon. It is therefore imperative that compute-bound algorithms are amenable to both multithreading and vectorisation. A versatile means of accomplishing this is by

breaking the computation down into multiple, necessarily independent, streams. By virtue of their independence these streams can be readily divided up between cores and vector lanes. This leads directly to the concept of *stream processing*. We will refer to architectures amenable to this form of parallelisation as streaming architectures.

A corollary of the above discussion is that compute intensive discretisations which can be formulated within the stream processing paradigm are well suited to acceleration on current—and likely future—hardware platforms. The FR approach combined with explicit time stepping is an archetypical of this.

Our objective in this paper is to present PyFR, an open-source Python based framework for solving advection-diffusion type problems on streaming architectures using the FR approach. The framework is designed to solve a range of governing systems on mixed unstructured grids containing various element types. It is also designed to target a range of hardware platforms via use of an in-built domain specific language derived from the Mako templating engine. The current release of PyFR is able to solve the compressible Euler and Navier-Stokes equations on unstructured grids of quadrilateral and triangular elements in two-dimensions, and unstructured grids of hexahedral elements in three-dimensions, targeting clusters of CPUs, and NVIDIA GPUs. The paper is structured as follows. In section 2 we provide a complete description of the FR approach for advection-diffusion type problems on mixed unstructured grids, detailing how the majority of mathematical operations map to a series of matrix multiplies. In section section 3 we proceed to describe our implementation strategy, and in section section 4 we describe the Euler and Navier-Stokes equations, which are solved by the current release of PyFR. The framework is then validated in section section 5, scaling results are presented in section section 6, and finally conclusions are drawn in section section 7.

2 Discretisation

2.1 Mathematical Formulation

Consider the following advection-diffusion problem inside an arbitrary domain Ω in N_D dimensions

$$\frac{\partial u_\alpha}{\partial t} + \nabla \cdot \mathbf{f}_\alpha = 0, \quad (1)$$

where $0 \leq \alpha < N_V$ is the *field variable* index, $u_\alpha = u_\alpha(\mathbf{x}, t)$ is a conserved quantity, $\mathbf{f}_\alpha = \mathbf{f}_\alpha(u, \nabla u)$ is the flux of this conserved quantity and $\mathbf{x} = x_i \in \mathbb{R}^{N_D}$. In defining the flux we have taken u in its unscripted form to refer to all of the N_V field variables and ∇u to be an object of length $N_D \times N_V$ consisting of the gradient of each field variable. We start by rewriting Equation 1 as a first order system

$$\frac{\partial u_\alpha}{\partial t} + \nabla \cdot \mathbf{f}_\alpha(u, \mathbf{q}) = 0, \quad (2a)$$

$$\mathbf{q}_\alpha - \nabla u_\alpha = 0, \quad (2b)$$

where \mathbf{q} is an auxiliary variable.

Take \mathcal{E} to be the set of available element types in \mathbb{R}^{N_D} . Example include quadrilaterals and triangles in two dimensions and hexahedra, prisms, pyramids and tetrahedra in three dimensions. Consider using these various elements types to construct a conformal mesh of the domain such that

$$\Omega = \bigcup_{e \in \mathcal{E}} \Omega_e \quad \text{and} \quad \Omega_e = \bigcup_{n=0}^{|\Omega_e|-1} \Omega_{en} \quad \text{and} \quad \bigcap_{e \in \mathcal{E}} \bigcap_{n=0}^{|\Omega_e|-1} \Omega_{en} = \emptyset,$$

where Ω_e refers to all of the elements of type e inside of the domain, $|\Omega_e|$ is the number of elements of this type in the decomposition, and n is an index running over these elements with $0 \leq n < |\Omega_e|$. Inside each element Ω_{en} we require that

$$\frac{\partial u_{en\alpha}}{\partial t} + \nabla \cdot \mathbf{f}_{en\alpha} = 0, \quad (3a)$$

$$\mathbf{q}_{en\alpha} - \nabla u_{en\alpha} = 0. \quad (3b)$$

It is convenient, for reasons of both mathematical simplicity and computational efficiency, to work in a transformed space. We accomplish this by introducing, for each element type, a standard element $\hat{\Omega}_e$ which exists in a transformed space, $\tilde{\mathbf{x}} = \tilde{x}_i$. Next, assume the existence of a mapping function for each element such that

$$\begin{aligned} x_i &= \mathcal{M}_{eni}(\tilde{\mathbf{x}}), & \mathbf{x} &= \mathcal{M}_{en}(\tilde{\mathbf{x}}), \\ \tilde{x}_i &= \mathcal{M}_{eni}^{-1}(\mathbf{x}), & \tilde{\mathbf{x}} &= \mathcal{M}_{en}^{-1}(\mathbf{x}), \end{aligned}$$

along with the relevant Jacobian matrices

$$\begin{aligned} \mathbf{J}_{en} &= J_{enij} = \frac{\partial \mathcal{M}_{eni}}{\partial \tilde{x}_j}, & J_{en} &= \det \mathbf{J}_{en}, \\ \mathbf{J}_{en}^{-1} &= J_{enij}^{-1} = \frac{\partial \mathcal{M}_{eni}^{-1}}{\partial x_j}, & J_{en}^{-1} &= \det \mathbf{J}_{en}^{-1} = \frac{1}{J_{en}}. \end{aligned}$$

These definitions provide us with a means of transforming quantities to and from standard element space. Taking the transformed solution, flux, and gradients inside each element to be

$$\tilde{u}_{en\alpha} = \tilde{u}_{en\alpha}(\tilde{\mathbf{x}}, t) = J_{en}(\tilde{\mathbf{x}}) u_{en\alpha}(\mathcal{M}_{en}(\tilde{\mathbf{x}}), t), \quad (4a)$$

$$\tilde{\mathbf{f}}_{en\alpha} = \tilde{\mathbf{f}}_{en\alpha}(\tilde{\mathbf{x}}, t) = J_{en}(\tilde{\mathbf{x}}) \mathbf{J}_{en}^{-1}(\mathcal{M}_{en}(\tilde{\mathbf{x}})) \mathbf{f}_{en\alpha}(\mathcal{M}_{en}(\tilde{\mathbf{x}}), t), \quad (4b)$$

$$\tilde{\mathbf{q}}_{en\alpha} = \tilde{\mathbf{q}}_{en\alpha}(\tilde{\mathbf{x}}, t) = \mathbf{J}_{en}^T(\tilde{\mathbf{x}}) \mathbf{q}_{en\alpha}(\mathcal{M}_{en}(\tilde{\mathbf{x}}), t), \quad (4c)$$

and letting $\tilde{\nabla} = \partial / \partial \tilde{x}_i$, it can be readily verified that

$$\frac{\partial \tilde{u}_{en\alpha}}{\partial t} + J_{en}^{-1} \tilde{\nabla} \cdot \tilde{\mathbf{f}}_{en\alpha} = 0, \quad (5a)$$

$$\tilde{\mathbf{q}}_{en\alpha} - \tilde{\nabla} \tilde{u}_{en\alpha} = 0, \quad (5b)$$

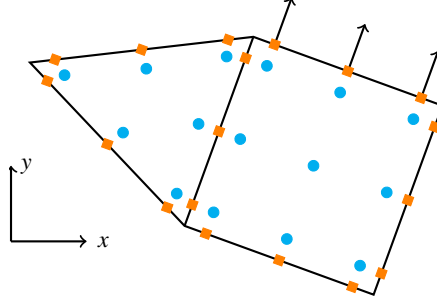


Figure 2. Solution points (blue circles) and flux points (orange squares) for a triangle and quadrangle in physical space. For the top edge of the quadrangle the normal vectors have been plotted. Observe how the flux points at the interface between the two elements match up.

as required. We note here the decision to multiply the first equation through by a factor of J_{en}^{-1} . Doing so has the effect of taking $\tilde{u}_{en} \mapsto u_{en}$ which allows us to work in terms of the physical solution. This is more convenient from a computational standpoint.

We next proceed to associate with each standard element a set of solution points. For each type $e \in \mathcal{E}$ take $\{\tilde{\mathbf{x}}_{e\rho}^{(u)}\}$ to be the chosen set of points where $0 \leq \rho < N_e^{(u)}(\wp)$. These points can then be used to construct a nodal basis set $\{\ell_{e\rho}^{(u)}(\tilde{\mathbf{x}})\}$ with the property that $\ell_{e\rho}^{(u)}(\tilde{\mathbf{x}}_{e\sigma}^{(u)}) = \delta_{\rho\sigma}$. To obtain such a set we first take $\{\psi_{e\sigma}(\tilde{\mathbf{x}})\}$ to be any basis which spans the order \wp polynomial space defined inside $\hat{\Omega}_e$. Next we compute the elements of the generalised Vandermonde matrix $\mathcal{V}_{e\rho\sigma} = \psi_{e\sigma}(\tilde{\mathbf{x}}_{e\rho}^{(u)})$. With these a nodal basis set can be constructed as $\ell_{e\rho}^{(u)}(\tilde{\mathbf{x}}) = \mathcal{V}_{e\rho\sigma}^{-1} \psi_{e\sigma}(\tilde{\mathbf{x}})$. Along with the solution points inside of each element we also define a set of flux points on $\partial\hat{\Omega}_e$. We denote the flux points for a particular element type as $\{\tilde{\mathbf{x}}_{e\rho}^{(f)}\}$ where $0 \leq \rho < N_e^{(f)}(\wp)$. Let the set of corresponding normalised outward-pointing normal vectors be given by $\{\hat{\mathbf{n}}_{e\rho}^{(f)}\}$. It is critical that each flux point pair along an interface share the same coordinates in physical space. For a pair of flux points $e\rho n$ and $e'\rho'n'$ at a non-periodic interface this can be formalised as $\mathcal{M}_{en}(\tilde{\mathbf{x}}_{e\rho}^{(f)}) = \mathcal{M}_{e'n'}(\tilde{\mathbf{x}}_{e'\rho'}^{(f)})$. A pictorial illustration of this can be seen in Figure 2.

The first step in the FR approach is to go from the discontinuous solution at the solution points to the discontinuous solution at the flux points

$$u_{e\sigma n\alpha}^{(f)} = u_{e\rho n\alpha}^{(u)} \ell_{e\rho}^{(u)}(\tilde{\mathbf{x}}_{e\sigma}^{(f)}), \quad (6)$$

where $u_{e\rho n\alpha}^{(u)}$ is an approximate solution of field variable α inside of the n th element of type e at solution point $\tilde{\mathbf{x}}_{e\rho}^{(u)}$. This can then be used to compute a *common interface solution*

$$\mathfrak{C}_\alpha u_{e\rho n\alpha}^{(f)} = \mathfrak{C}_\alpha u_{e\rho n\alpha}^{(f)} = \mathfrak{C}_\alpha (u_{e\rho n\alpha}^{(f)}, u_{e\rho n\alpha}^{(f)}), \quad (7)$$

where $\mathfrak{C}_\alpha(u_L, u_R)$ is a scalar function that given two values at a point returns a common value. Here we have taken $\widetilde{e\rho n}$ to be the element type, flux point number

and element number of the adjoining point at the interface. Since grids in FR are permitted to be unstructured the relationship between epn and \widetilde{epn} is indirect. This necessitates the use of a lookup table. As the common solution function is permitted to perform upwinding or downwinding of the solution it is in general the case that $\mathfrak{C}_\alpha(u_{epn\alpha}^{(f)}, u_{\widetilde{epn\alpha}}^{(f)}) \neq \mathfrak{C}_\alpha(u_{\widetilde{epn\alpha}}^{(f)}, u_{epn\alpha}^{(f)})$. Hence, it is important that each flux point pair only be visited *once* with the same common solution value assigned to both $\mathfrak{C}_\alpha u_{epn\alpha}^{(f)}$ and $\mathfrak{C}_\alpha u_{\widetilde{epn\alpha}}^{(f)}$.

Further, associated with each flux point is a vector correction field $\mathbf{g}_{ep}^{(f)}(\tilde{\mathbf{x}})$ constrained such that

$$\hat{\mathbf{n}}_{e\sigma}^{(f)} \cdot \mathbf{g}_{ep}^{(f)}(\tilde{\mathbf{x}}_{e\sigma}^{(f)}) = \delta_{\rho\sigma}, \quad (8)$$

with a divergence that sits in the same polynomial space as the solution. Using these fields we can express the solution to Equation 5b as

$$\tilde{\mathbf{q}}_{e\sigma n\alpha}^{(u)} = \left[\hat{\mathbf{n}}_{ep}^{(f)} \cdot \tilde{\nabla} \cdot \mathbf{g}_{ep}^{(f)}(\tilde{\mathbf{x}}) \{ \mathfrak{C}_\alpha u_{epn\alpha}^{(f)} - u_{epn\alpha}^{(f)} \} + u_{evn\alpha}^{(u)} \tilde{\nabla} \ell_{ev}^{(u)}(\tilde{\mathbf{x}}) \right]_{\tilde{\mathbf{x}}=\tilde{\mathbf{x}}_{e\sigma}^{(u)}}, \quad (9)$$

where the term inside the curly brackets is the ‘jump’ at the interface and the final term is an order $\varphi - 1$ approximation of the gradient obtained by differentiating the discontinuous solution polynomial. Following the approaches of Kopriva [9] and Sun et al. [6] we can now compute physical gradients as

$$\mathbf{q}_{e\sigma n\alpha}^{(u)} = \mathbf{J}_{e\sigma n}^{-T(u)} \tilde{\mathbf{q}}_{e\sigma n\alpha}^{(u)}, \quad (10)$$

$$\mathbf{q}_{e\sigma n\alpha}^{(f)} = \ell_{ep}^{(u)}(\tilde{\mathbf{x}}_{e\sigma}^{(f)}) \mathbf{q}_{epn\alpha}^{(u)}, \quad (11)$$

where $\mathbf{J}_{e\sigma n}^{-T(u)} = \mathbf{J}_{en}^{-T}(\tilde{\mathbf{x}}_{e\sigma}^{(u)})$. Having solved the auxiliary equation we are now able to evaluate the transformed flux

$$\tilde{\mathbf{f}}_{epn\alpha}^{(u)} = J_{epn}^{(u)} \mathbf{J}_{epn}^{-1(u)} \mathbf{f}_\alpha(u_{epn}, \mathbf{q}_{epn}^{(u)}), \quad (12)$$

where $J_{epn}^{(u)} = \det \mathbf{J}_{en}(\tilde{\mathbf{x}}_{ep}^{(u)})$. This can be seen to be a collocation projection of the flux. With this it is possible to compute the normal transformed flux at each of the flux points

$$\tilde{f}_{e\sigma n\alpha}^{(f_\perp)} = \ell_{ep}^{(u)}(\tilde{\mathbf{x}}_{e\sigma}^{(f)}) \hat{\mathbf{n}}_{e\sigma}^{(f)} \cdot \tilde{\mathbf{f}}_{epn\alpha}^{(u)}. \quad (13)$$

Considering the physical normals at the flux points we see that

$$\mathbf{n}_{e\sigma n}^{(f)} = n_{e\sigma n}^{(f)} \hat{\mathbf{n}}_{e\sigma n}^{(f)} = \mathbf{J}_{e\sigma n}^{-T(f)} \hat{\mathbf{n}}_{e\sigma}^{(f)}, \quad (14)$$

which is the outward facing normal vector in physical space where $n_{e\sigma n}^{(f)} > 0$ is defined as the magnitude. As the interfaces between two elements conform we must have $\hat{\mathbf{n}}_{e\sigma n}^{(f)} = -\hat{\mathbf{n}}_{e\sigma n}^{(f)}$. With these definitions we are now in a position to specify an expression for the *common normal flux* at a flux point pair as

$$\tilde{\mathfrak{F}}_\alpha f_{e\sigma n\alpha}^{(f_\perp)} = -\tilde{\mathfrak{F}}_\alpha f_{\widetilde{e\sigma n\alpha}}^{(f_\perp)} = \tilde{\mathfrak{F}}_\alpha (u_{e\sigma n}^{(f)}, u_{\widetilde{e\sigma n}}^{(f)}, \mathbf{q}_{e\sigma n}^{(f)}, \mathbf{q}_{\widetilde{e\sigma n}}^{(f)}, \hat{\mathbf{n}}_{e\sigma n}^{(f)}). \quad (15)$$

The relationship $\tilde{\mathcal{F}}_\alpha f_{e\sigma n\alpha}^{(f_\perp)} = -\tilde{\mathcal{F}}_\alpha f_{e\sigma n\alpha}^{(f_\perp)}$ arises from the desire for the resulting numerical scheme to be conservative; a net outward flux from one element must be balanced by a corresponding inward flux on the adjoining element. It follows that that $\tilde{\mathcal{F}}_\alpha(u_L, u_R, \mathbf{q}_L, \mathbf{q}_R, \hat{\mathbf{n}}_L) = -\tilde{\mathcal{F}}_\alpha(u_R, u_L, \mathbf{q}_R, \mathbf{q}_L, -\hat{\mathbf{n}}_L)$. The common normal fluxes in Equation 15 can now be taken into transformed space via

$$\tilde{\mathcal{F}}_\alpha \tilde{f}_{e\sigma n\alpha}^{(f_\perp)} = J_{e\sigma n}^{(f)} n_{e\sigma n}^{(f)} \tilde{\mathcal{F}}_\alpha f_{e\sigma n\alpha}^{(f_\perp)}, \quad (16)$$

$$\tilde{\mathcal{F}}_\alpha \tilde{f}_{e\sigma n\alpha}^{(f_\perp)} = J_{e\sigma n}^{(f)} n_{e\sigma n}^{(f)} \tilde{\mathcal{F}}_\alpha f_{e\sigma n\alpha}^{(f_\perp)}, \quad (17)$$

where $J_{e\sigma n}^{(f)} = \det \mathbf{J}_{en}(\tilde{\mathbf{x}}_{e\sigma}^{(f)})$.

It is now possible to compute an approximation for the divergence of the *continuous* flux. The procedure is directly analogous to the one used to calculate the transformed gradient in Equation 9

$$(\tilde{\nabla} \cdot \tilde{\mathbf{f}})_{epn\alpha}^{(u)} = \left[\tilde{\nabla} \cdot \mathbf{g}_{e\sigma}^{(f)}(\tilde{\mathbf{x}}) \{ \tilde{\mathcal{F}}_\alpha \tilde{f}_{e\sigma n\alpha}^{(f_\perp)} - \tilde{f}_{e\sigma n\alpha}^{(f_\perp)} \} + \tilde{\mathbf{f}}_{evn\alpha}^{(u)} \cdot \tilde{\nabla} \ell_{ev}^{(u)}(\tilde{\mathbf{x}}) \right]_{\tilde{\mathbf{x}}=\tilde{\mathbf{x}}_{ep}^{(u)}}, \quad (18)$$

which can then be used to obtain a semi-discretised form of the governing system

$$\frac{\partial u_{epn\alpha}^{(u)}}{\partial t} = -J_{epn}^{-1(u)} (\tilde{\nabla} \cdot \tilde{\mathbf{f}})_{epn\alpha}^{(u)}, \quad (19)$$

where $J_{epn}^{-1(u)} = \det \mathbf{J}_{en}^{-1}(\tilde{\mathbf{x}}_{ep}^{(u)}) = 1/J_{epn}^{(u)}$. This semi-discretised form is simply a system of ordinary differential equations in t and can be solved using one of a number of schemes, e.g. RK4.

2.2 Matrix Representation

It is possible to cast many of the operations in an FR step as matrix-matrix multiplications of the form

$$\mathbf{C} \leftarrow c_1 \mathbf{A} \mathbf{B} + c_2 \mathbf{C}, \quad (20)$$

where $c_{1,2} \in \mathbb{R}$ are constants, \mathbf{A} is a constant operator matrix, and \mathbf{B} and \mathbf{C} are state matrices. The utility of this representation arises from the fact that high performance matrix multiplication kernels are available for virtually all hardware platforms. Indeed, such multiplications are often to obtain extremely high fraction of R_{peak} with well-understood performance profiles. Hence, by expressing FR in terms of matrix-matrix multiplication operations it is possible to offload many of the intricacies associated with a given platform to the vendor-provided Basic Linear Algebra Subprograms (BLAS) library. To accomplish this we start by introducing the following matrices

$$\begin{aligned} (\mathbf{M}_e^0)_{\sigma\rho} &= \ell_{ep}^{(u)}(\tilde{\mathbf{x}}_{e\sigma}^{(f)}), & \dim \mathbf{M}_e^0 &= N_e^{(f)} \times N_e^{(u)}, \\ (\mathbf{U}_e^{(u)})_{\rho(n\alpha)} &= u_{epn\alpha}^{(u)}, & \dim \mathbf{U}_e^{(u)} &= N_e^{(u)} \times N_V |\Omega_e|, \\ (\mathbf{U}_e^{(f)})_{\sigma(n\alpha)} &= u_{e\sigma n\alpha}^{(f)}, & \dim \mathbf{U}_e^{(f)} &= N_e^{(f)} \times N_V |\Omega_e|. \end{aligned}$$

In specifying the solution matrices there is a degree of freedom regarding how the field variables of the various elements are packed along a row. The packing of field variables can be characterised by considering the distance, Δj , in columns between two subsequent field variables for a given element. The case of $\Delta j = 1$ corresponds to the array of structures (AoS) packing whereas the choice of $\Delta j = |\mathbf{\Omega}_e|$ leads to the structure of arrays (SoA) packing. A hybrid approach wherein $\Delta j = k$ with k being constant results in the AoSoA(k) approach. An implementation is free to choose between any of these counting patterns so long as it is consistent. Using these matrices we are able to reformulate Equation 6 as

$$\mathbf{U}_e^{(f)} = \mathbf{M}_e^0 \mathbf{U}_e^{(u)}. \quad (21)$$

To apply a similar procedure to Equation 9 we let

$$\begin{aligned} (\mathbf{M}_e^4)_{\rho\sigma} &= [\tilde{\nabla} \ell_{ep}^{(u)}(\tilde{\mathbf{x}})]_{\tilde{\mathbf{x}}=\tilde{\mathbf{x}}_{e\sigma}^{(u)}}, & \dim \mathbf{M}_e^4 &= N_D N_e^{(u)} \times N_e^{(u)}, \\ (\mathbf{M}_e^6)_{\rho\sigma} &= [\hat{\mathbf{n}}_{ep}^{(f)} \cdot \tilde{\nabla} \cdot \mathbf{g}_{ep}^{(f)}(\tilde{\mathbf{x}})]_{\tilde{\mathbf{x}}=\tilde{\mathbf{x}}_{e\sigma}^{(f)}}, & \dim \mathbf{M}_e^6 &= N_D N_e^{(u)} \times N_e^f, \\ (\mathbf{C}_e^{(f)})_{\rho(n\alpha)} &= \mathfrak{C}_\alpha u_{epn\alpha}^{(f)}, & \dim \mathbf{C}_e^{(f)} &= N_e^{(f)} \times N_V |\mathbf{\Omega}_e|, \\ (\tilde{\mathbf{Q}}_e^{(u)})_{\sigma(n\alpha)} &= \tilde{\mathbf{q}}_{e\sigma n\alpha}^{(u)}, & \dim \tilde{\mathbf{Q}}_e^{(u)} &= N_D N_e^{(u)} \times N_V |\mathbf{\Omega}_e|, \end{aligned}$$

Here it is important to qualify assignments of the form $\mathbf{A}_{ij} = \mathbf{x}$ where \mathbf{x} is a N_D component vector. As above there is a degree of freedom associated with the packing. With the benefit of foresight we take the offset between dimensions in a matrix column to be either $\Delta i = N_e^{(u)}$ or $\Delta i = N_e^{(f)}$ depending on the context. With these matrices Equation 9 reduces to

$$\begin{aligned} \tilde{\mathbf{Q}}_e^{(u)} &= \mathbf{M}_e^6 \{\mathbf{C}_e^{(f)} - \mathbf{U}_e^{(f)}\} + \mathbf{M}_e^4 \mathbf{U}_e^{(u)} \\ &= \mathbf{M}_e^6 \{\mathbf{C}_e^{(f)} - \mathbf{M}_e^0 \mathbf{U}_e^{(u)}\} + \mathbf{M}_e^4 \mathbf{U}_e^{(u)} \\ &= \mathbf{M}_e^6 \mathbf{C}_e^{(f)} + \{\mathbf{M}_e^4 - \mathbf{M}_e^6 \mathbf{M}_e^0\} \mathbf{U}_e^{(u)}. \end{aligned} \quad (22)$$

Applying the procedure to Equation 11 we take

$$\begin{aligned} \mathbf{M}_e^5 &= \text{diag}(\mathbf{M}_e^0, \dots, \mathbf{M}_e^0) & \dim \mathbf{M}_e^5 &= N_D N_e^{(f)} \times N_D N_e^{(u)}, \\ (\mathbf{Q}_e^{(u)})_{\sigma(n\alpha)} &= \mathbf{q}_{e\sigma n\alpha}^{(u)}, & \dim \mathbf{Q}_e^{(u)} &= N_D N_e^{(u)} \times N_V |\mathbf{\Omega}_e|, \\ (\mathbf{Q}_e^{(f)})_{\sigma(n\alpha)} &= \mathbf{q}_{e\sigma n\alpha}^{(f)}, & \dim \mathbf{Q}_e^{(f)} &= N_D N_e^{(f)} \times N_V |\mathbf{\Omega}_e|, \end{aligned}$$

hence

$$\tilde{\mathbf{Q}}_e^{(f)} = \mathbf{M}_e^5 \mathbf{Q}_e^{(u)}, \quad (23)$$

where we note the block diagonal structure of \mathbf{M}_e^5 . This is a direct consequence of the above choices for Δi . Finally, to rewrite Equation 18 we write

$$\begin{aligned}
(\mathbf{M}_e^1)_{\rho\sigma} &= [\tilde{\nabla} \ell_{e\rho}^{(u)}(\tilde{\mathbf{x}})]_{\tilde{\mathbf{x}}=\tilde{\mathbf{x}}_{e\sigma}^{(u)}}^T, & \dim \mathbf{M}_e^1 &= N_e^{(u)} \times N_D N_e^{(u)}, \\
(\mathbf{M}_e^2)_{\rho\sigma} &= [\ell_{e\rho}^{(u)}(\tilde{\mathbf{x}}_{e\sigma}^{(f)}) \hat{\mathbf{n}}_{e\sigma}^{(f)}]^T, & \dim \mathbf{M}_e^2 &= N_e^{(f)} \times N_D N_e^{(u)}, \\
(\mathbf{M}_e^3)_{\rho\sigma} &= [\tilde{\nabla} \cdot \mathbf{g}_{e\sigma}^{(f)}(\tilde{\mathbf{x}})]_{\tilde{\mathbf{x}}=\tilde{\mathbf{x}}_{e\rho}^{(u)}}, & \dim \mathbf{M}_e^3 &= N_e^{(u)} \times N_e^{(f)}, \\
(\tilde{\mathbf{D}}_e^{(f)})_{\sigma(n\alpha)} &= \tilde{\mathfrak{F}}_\alpha \tilde{f}_{e\sigma n\alpha}^{(f_\perp)}, & \dim \tilde{\mathbf{D}}_e^{(f)} &= N_e^{(f)} \times N_V |\Omega_e|, \\
(\tilde{\mathbf{F}}_e^{(u)})_{\rho(n\alpha)} &= \tilde{\mathbf{f}}_{e\rho n\alpha}^{(u)}, & \dim \tilde{\mathbf{F}}_e^{(u)} &= N_D N_e^{(u)} \times N_V |\Omega_e|, \\
(\tilde{\mathbf{R}}_e^{(u)})_{\rho(n\alpha)} &= (\tilde{\nabla} \cdot \tilde{\mathbf{f}})_{e\rho n\alpha}^{(u)}, & \dim \tilde{\mathbf{R}}_e^{(u)} &= N_e^{(u)} \times N_V |\Omega_e|,
\end{aligned}$$

and after substitution of Equation 13 for $\tilde{f}_{e\sigma n\alpha}^{(f_\perp)}$ obtain

$$\begin{aligned}
\tilde{\mathbf{R}}_e^{(u)} &= \mathbf{M}_e^3 \{ \tilde{\mathbf{D}}_e^{(f)} - \mathbf{M}_e^2 \tilde{\mathbf{F}}_e^{(u)} \} + \mathbf{M}_e^1 \tilde{\mathbf{F}}_e^{(u)} \\
&= \mathbf{M}_e^3 \tilde{\mathbf{D}}_e^{(f)} + \{ \mathbf{M}_e^1 - \mathbf{M}_e^3 \mathbf{M}_e^2 \} \tilde{\mathbf{F}}_e^{(u)}.
\end{aligned} \tag{24}$$

2.3 Parameterisation

The behaviour of an FR scheme for advection-diffusion type problems is determined by the following parameters: the polynomial order φ ; the location of the solution points $\{\tilde{\mathbf{x}}_{e\rho}^{(u)}\}$ and the flux points $\{\tilde{\mathbf{x}}_{e\rho}^{(f)}\}$; the form of the correction fields $\{\mathbf{g}_{e\rho}^{(f)}\}$, inside each standard element; and the methodology for computing the common solutions \mathfrak{C}_α and normal fluxes $\tilde{\mathfrak{F}}_\alpha$ between pairs of flux points. Whereas φ , \mathfrak{C}_α , and $\tilde{\mathfrak{F}}_\alpha$ are independent of element type $\{\tilde{\mathbf{x}}_{e\rho}^{(u)}\}$, $\{\tilde{\mathbf{x}}_{e\rho}^{(f)}\}$, and $\{\mathbf{g}_{e\rho}^{(f)}\}$ are not. In this section we will provide a brief overview of how these can be specified for various finite element types. To simplify the presentation we make the observation that within the FR approach for advection-diffusion type problems that the correction fields are never utilised directly. In both Equation 9 and Equation 18 it is the *divergence* of these fields which is applied. Hence, it is sufficient for an element type to define $\{\nabla \cdot \mathbf{g}_{e\rho}^{(f)}\}$ in lieu of $\{\mathbf{g}_{e\rho}^{(f)}\}$. Furthermore, instead of using element wide flux point numbers, as denoted by ρ , it is often more convenient to use a face-local numbering scheme. In such a scheme a flux point is indexed by an edge/face number i and a local index j . It follows that $\rho \leftrightarrow (ij)$.

Line segments. In the case of a one dimensional line segment we take a standard line to be defined as $\tilde{x} \in [-1, 1]$. To specify an order φ polynomial inside of this segment it is clear that $\varphi + 1$ points are required. Hence $N_p^{(u)} = \varphi + 1$. From the topology it is evident that the flux points must be at $\{-1, 1\}$ with $N_p^{(f)} = 2$. Keeping with convention we will denote the correction functions associated with the flux points as g_L and g_R , respectively. In his seminal paper on FR Huynh [7] showed that through a judicious choice of correction functions one could recover a collocation nodal DG as specified in [8] and (for a linear flux function) any spectral difference

(SD) scheme. Moreover, Huynh also proposed several new high-order schemes. Of particular note is the ‘ g_2 ’ scheme which was found to have a somewhat relaxed CFL limit. In 2011 Vincent et al. [10] used an ‘energy method’ to discover an infinite range of linearly stable FR schemes parameterised by a single scalar. Herein referred to as Vincent-Castonguay-Jameson-Huynh (VCJH) schemes the correction functions are given by

$$g_L(\tilde{x}) = -g_R(-\tilde{x}) \quad \text{and} \quad g_R(\tilde{x}) = \frac{1}{2} \left[P_\varphi - \left(\frac{\eta P_{\varphi-1} + P_{\varphi+1}}{1 + \eta} \right) \right], \quad (25)$$

where P_φ is an order φ Legendre polynomial in \tilde{x} and η a constant. Special values for η are: zero which corresponds to a DG scheme, $\varphi/(\varphi+1)$ which gives a particular SD scheme, and $(\varphi+1)/\varphi$ which yields Huynh’s g_2 approach (HU).

While investigating the non-linear stability of FR schemes Jameson et al. [11] found that the degree of aliasing driven instabilities depends upon the location of the solution points. Specifically, it has been found that placing points at the abscissa of strong Gaussian quadrature rules has a positive impact on the performance of the resulting scheme. Given this the solution points are normally taken to be at either Gauss-Legendre or Gauss-Legendre-Lobatto points. These rule sets are of quadrature strength $2\varphi+1$ and $2\varphi-1$, respectively.

Quadrangles and hexahedra. The FR approach can be readily extended to quadrilaterals and hexahedra via the construction of tensor product bases [7, 12]. Solution points are given by a Cartesian power of a set of one dimensional solution points $\{\tilde{x}_\rho^{(u)}\}^{N_D}$ with $N_D \in \{2, 3\}$ and $N^{(u)} = (\varphi+1)^{N_D}$. For quadrilaterals flux points are obtained by projecting the set of $\{\tilde{x}_p^{(u)}\}$ onto each of the four edges. Analogously, in hexahedra, the flux points are given by the projection of $\{\tilde{x}_p^{(u)}\}^2$ onto each of the six quadrilateral faces. Hence $N^{(f)} = 2N_D(\varphi+1)^{N_D-1}$. The correction fields in tensor product elements are given by

$$\nabla \cdot \mathbf{g}_{(ij)}^{(f)}(\tilde{\mathbf{x}}) = \ell_{ij}(\tilde{\mathbf{x}}) g'_R(\hat{\mathbf{n}}_{ij} \cdot \tilde{\mathbf{x}}), \quad (26)$$

where $\ell_{ij}(\tilde{\mathbf{x}})$ is a nodal basis on face i of the element with the property that $\ell_{ij}(\tilde{\mathbf{x}}_{ik}) = \delta_{jk}$. Note that the stability of these schemes in the case of $\eta \neq 0$ has yet to be demonstrated.

Triangles. A range of VCJH-like schemes for triangular elements was introduced by Castonguay et al. [13]. As with one dimensional line segments it is possible to recover a collocation based nodal DG method. To accomplish this we first introduce an orthonormal basis $\{\psi_\rho(\tilde{\mathbf{x}})\}$ inside of our reference triangle with the property that

$$\iint_{\hat{\Omega}} \psi_\rho(\tilde{\mathbf{x}}) \psi_\sigma(\tilde{\mathbf{x}}) d^2 \tilde{\mathbf{x}} = \delta_{\rho\sigma}, \quad (27)$$

and further let $\{\tilde{\Gamma}_i\}$ refer to the three edges of the reference triangle. With these we can express the divergences of set of correction fields recovering a DG scheme as

$$\nabla \cdot \mathbf{g}_{(ij)}^{(f)}(\tilde{\mathbf{x}}) = \psi_k(\tilde{\mathbf{x}}) \int_{\tilde{\Gamma}_i} \hat{\mathbf{n}} \cdot \mathbf{g}_{(ij)}^{(f)}(\tilde{\mathbf{s}}) \psi_k(\tilde{\mathbf{s}}) d\tilde{\mathbf{s}}, \quad (28)$$

where $\hat{\mathbf{n}}$ is the outward pointing unit normal vector along the edge. Since Equation 8 requires that $\hat{\mathbf{n}}_{\sigma}^{(f)} \cdot \mathbf{g}_{\rho}^{(f)}(\tilde{\mathbf{x}}_{\sigma}^{(f)}) = \delta_{\rho\sigma}$ it is clear that when integrating along an edge that this constraint fixes $\hat{\mathbf{n}} \cdot \mathbf{g}_{(ij)}^{(f)}$ at $N^{(f)}/3$ points. It can be shown [13] that this is sufficient to completely define the above expression along an edge. Hence we can write

$$\nabla \cdot \mathbf{g}_{(ij)}^{(f)}(\tilde{\mathbf{x}}) = \psi_k(\tilde{\mathbf{x}}) \int_{\tilde{\Gamma}_i} \ell_{ij}(\tilde{\mathbf{s}}) \psi_k(\tilde{\mathbf{s}}) d\tilde{\mathbf{s}}, \quad (29)$$

where $\ell_{ij}(\tilde{\mathbf{s}})$ is a one dimensional nodal basis polynomial with the property that $\ell_{ij}(\tilde{\mathbf{x}}_{(ik)}^{(f)}) = \delta_{jk}$. The extended range of energy stable VCJH schemes can be recovered in one of two ways. The first method, as proposed by Castonguay et al. [13] is through a more general form of the procedure sketched above. More recently, Williams [12] has shown that it is possible to view these extended schemes as a form of filtered DG. Within this filtering framework one uses the DG correction fields as a starting point and then constructs a filter which when applied to these fields yields an extended scheme.

Inside of a triangle $N^{(u)} = (\varphi + 1)(\varphi + 2)/2$ and $N^{(f)} = 3(\varphi + 1)$. As with quadrilaterals the set of flux points are obtained by projecting a set of one dimensional solution points $\{\tilde{x}_p^{(u)}\}$ onto each edge. For mixed element meshes this set of points must be the same as those used for quadrilaterals. The placement of solution points inside of a triangle is still an area of open research. Unlike in the tensor product elements—where the solution points are given as the roots of orthogonal polynomials—in triangles points are obtained through various optimisation procedures and must be tabulated for each φ . A comparison of various point sets by Witherden and Vincent [14] found that the Williams-Shunn points of [12] are a reasonable choice and further reaffirmed the notion that it is important for the points to be at the abscissa of quadrature rules.

Tetrahedra. By following a procedure analogous to that in triangles Williams and Jameson [15] were able to derive a range of energy stable schemes in tetrahedra. For tets $N^{(u)} = (\varphi + 1)(\varphi + 2)(\varphi + 3)/6$ and $N^{(f)} = 2(\varphi + 1)(\varphi + 2)$ with the flux points being obtained by projecting a set of triangular solution points onto each of the four faces. A comparison of solution point sets by Williams and Jameson [16] found that the quadrature rules of Shunn and Ham [17] significantly outperformed the α -optimised points of Hesthaven and Warburton [8].

Prisms. The FR approach has also been extended via a tensor product construction of a line segment with a triangle to prismatic elements [18]. In such elements $N^{(u)} = (\varphi + 1)^2(\varphi + 2)/2$ and $N^{(f)} = (4\varphi + 5)(\varphi + 1)$. As in the case of quadrilaterals

and hexahedra the stability of the resulting scheme, which is parameterised by two scalars, has yet to be demonstrated except when both correction fields recover DG.

2.4 Boundary Conditions

To incorporate boundary conditions into the FR approach we introduce a set of boundary interface types $b \in \mathcal{B}$. At a boundary interface there is only a single flux point: that which belongs to the element whose edge/face is on the boundary. Associated with each boundary type are a pair of functions $\mathfrak{C}_\alpha^{(b)}(u_L)$ and $\mathfrak{F}_\alpha^{(b)}(u_L, \mathbf{q}_L, \hat{\mathbf{n}}_L)$ where u_L , \mathbf{q}_L , and $\hat{\mathbf{n}}_L$ are the solution, solution gradient and unit normals at the relevant flux point. These functions prescribe the common solutions and normal fluxes, respectively.

Instead of directly imposing solutions and normal fluxes it is oftentimes more convenient for a boundary to instead provide ghost states. In its simplest formulation $\mathfrak{C}_\alpha^{(b)} = \mathfrak{C}_\alpha(u_L, \mathfrak{B}^{(b)}u_L)$ and $\mathfrak{F}_\alpha^{(b)} = \mathfrak{F}_\alpha(u_L, \mathfrak{B}^{(b)}u_L, \mathbf{q}_L, \mathfrak{B}^{(b)}\mathbf{q}_L, \hat{\mathbf{n}}_L)$ where $\mathfrak{B}^{(b)}u_L$ is the ghost solution state and $\mathfrak{B}^{(b)}\mathbf{q}_L$ is the ghost solution gradient. It is straightforward to extend this prescription to allow for the provisioning of different ghost solution states for \mathfrak{C}_α and \mathfrak{F}_α and to permit $\mathfrak{B}^{(b)}\mathbf{q}_L$ to be a function of u_L in addition to \mathbf{q}_L .

2.5 Parallelism

The operations within an FR step can be separated into two categories: matrix multiplications and pointwise operations. A defining property of these pointwise operations is that they are localised to either a given solution point or pair of flux points. This localisation permits such operations to be trivially parallelised. Similarly, the matrix multiply stages are amenable to parallelisation through a variety of techniques. These properties lead to the FR approach being extremely well suited to platforms with a uniform memory architecture—including accelerators. However, to scale out past a single processor or GPU it is necessary to contend with memory architectures which are either non-uniform or distributed in nature. It is possible to incorporate support for such architectures into the FR approach with only minor modifications.

We begin by partitioning the mesh into regions. This partitioning results in there being two types of interfaces between elements: internal and external. In an internal interface both elements belong to the same region and as such the information associated with both of the flux points is available immediately. An external interface is one where the two elements belong to different regions. In such instances only half of the information is available immediately. The other half must be requested from the abutting region. Servicing such requests requires coordination from both regions and can incur a serious latency penalty. To mitigate these factors we note that in FR the data which must be exchanged between regions is the same each time step. Since this is known in advanced it is possible for regions to begin exchanging data with one another *before* it is required. This permits the overlapping of communication with computation.

As a concrete example we consider the computation of \mathcal{C}_α in Equation 7. This expression depends on the interpolated solution at each flux point, as computed by Equation 21. Hence, it is possible to begin exchanging interpolated solutions immediately after its evaluation. While this is occurring we can evaluate both the common interface solutions for the internal interfaces and the second term on the right hand side of Equation 22. Once this exchange has finished the remaining common interface solutions for the external interfaces can be calculated. With these we can then proceed to evaluate the remaining term in Equation 22 to yield the transformed gradient at the solution points. This procedure can also be applied to the computation of $\tilde{\mathcal{F}}_\alpha$ in Equation 15 where it is necessary to exchange interpolated gradients at the flux points.

3 Implementation

In broad terms an FR code can be decomposed into three main parts. The first of these involves computing the seven operator matrices introduced in subsection 2.2 for each of the element types in the mesh. Elements of these matrices are obtained by constructing and evaluating various polynomials at the solution/flux points. These polynomials are specified in terms of the nodal basis, gradients thereof, and divergences of the correction fields. Depending on the element type the expressions for these fields, as presented in subsection 2.3, can require the evaluation and integration of various polynomials. Since these operations are performed only at start up they are not speed critical. Part two is comprised of obtaining a performant matrix-matrix multiplication routine. Usually this is accomplished through the GEMM family of subroutines from BLAS. Highly optimised BLAS libraries are available for virtually all platforms and are oftentimes maintained by the hardware vendor themselves. The third and final part pertains to implementing the remaining (pointwise) operations. Such operations generally depend on the governing system being solved, the number of dimensions it is being solved in, and the target hardware platform.

Although conceptually simple both the first and third tasks can be challenging to code. While orthogonal and nodal polynomials are mathematically convenient they are far more difficult to evaluate and manipulate numerically. Care must be taken to ensure that all intermediate results are numerically stable and free from catastrophic cancellation. This is especially important when taking integrals or differentials. Another challenge pertains to implementation of the pointwise kernels: looking at Table 1 we note that there is no single parallel programming module that has full support across all current architectures. Hence, in order to target a wide range of hardware platforms it is necessary to provide multiple implementations of the pointwise kernels. This can quickly become burdensome.

Our code, PyFR, addresses both of these issues. Written primarily in the Python programming languages it is a complete multidimensional massively parallel flux reconstruction solver. To tackle the issue of having to manipulate a wide range of

Table 1. Comparison of different parallel programming models on common hardware platforms. Secondary support is used to indicate that a given model is not a primary focus. Models where implementations are in beta are categorised as unsupported.

	CUDA	OpenCL	OpenMP 3.1	OpenACC
x86 CPU	∅	⊠	★	★
Other CPU	∅	⊠	★	∅
Intel Xeon Phi	∅	∅	★	∅
NVIDIA GPU	★	⊠	∅	★
AMD GPU	∅	★	∅	∅

★ = supported ⊠ = secondary support ∅ = unsupported

polynomials PyFR makes extensive use of symbolic manipulation. This is accomplished through a library called SymPy [19] which brings computer algebra facilities similar to those found in Maple and Mathematica to Python. SymPy has built-in support for most common polynomials and can readily evaluate such expressions to arbitrary precision. Within PyFR support for multiple hardware architectures is accomplished through a series of *backends*. Currently there exist backends for CUDA via the wrapper PyCUDA [20] and C/OpenMP. Each backend implements a common interface which is based around two core data types: matrices and views. A view can be thought of as an array of pointers to elements in other matrices. These data types are operated on by *kernels*. Kernels can be either intrinsic or extrinsic. Intrinsic kernels are those which are provided by the backend and include core operations such as matrix multiplication and addition. The implementation of these kernels is almost always deferred to the platforms BLAS library. Conversely, an extrinsic kernel is one provided by the governing system. Such kernels are specified in a backend independent fashion using a domain specific language implemented atop of the Mako templating engine [21].

As an example of an extrinsic kernel we consider the evaluation of the right hand side of Equation 19, which reads $-J_{epn}^{-1(u)}(\tilde{\nabla} \cdot \tilde{\mathbf{f}})_{epn\alpha}^{(u)}$. The operation consists of a pointwise multiplication between the negative reciprocal of the Jacobian and the transformed divergence of the flux at each solution point. Figure 3 shows how such a kernel can be expressed in the domain specific language of PyFR. There are several points of consideration. Firstly, we note the purely scalar nature of the kernel. This is by design; in PyFR extrinsic kernels need only prescribe the pointwise operation to be applied. Important choices such as how to vectorise a given operation or how to gather data from memory are all delegated to the backend. It is, hence, completely possible for backends to use different data packing schemes without affecting the validity of any the extrinsic kernels. A second noteworthy aspect of the language is the ability to utilise Python when generating the main body of kernels. This capability is showcased on lines four, five and six where it is used to unroll a for


```

1 <%pyfr:kernel name='negdivconf' ndim='2'
2             tdivtconf='inout fpdtype_t[ $\{\text{str}(nvars)\}$ ]'
3             rcpdjac='in fpdtype_t'>
4 % for i in range(nvars):
5     tdivtconf[ $\{i\}$ ] *= -rcpdjac;
6 % endfor
7 </%pyfr:kernel>

```

Figure 3. An example of an extrinsic kernel in PyFR. The template variable $nvars$ is taken to be the number of field variables, N_v . The kernel arguments $tdivtconf$ and $rcpdjac$ correspond to $\tilde{\nabla} \cdot \tilde{\mathbf{f}}$ and J^{-1} respectively with the operation being performed in-place.

Table 2. Functionality implemented in PyFR.

Dimensions	2D, 3D
Precisions	Single, Double
Backends	CUDA, C/OpenMP
Communication	MPI
Elements	Tri, Quad, Hex
Spatial orders	Arbitrary
Time steppers	Euler, RK4, DOPRI5

loop over each of the field variables. Finally, we also highlight the use of an abstract data type $fpdtype_t$ for floating point variables which permits a single set of kernels to be used for both single and double precision operation. The generated CUDA source for this kernel can be seen in Figure 4 whereas the equivalent C kernel can be found in Figure 5. All extrinsic kernels are generated, compiled, linked and loaded at run-time. Consequently, extrinsic kernels are ephemeral and thus only need to function on the hardware which PyFR is currently running on. It is therefore possible during the compilation phase to instruct the compiler to emit binaries which are optimised for the current hardware architecture. Such optimisations can result in anything up to a fourfold improvement in performance when compared with architectural defaults.

For simplicity PyFR uses the SoA packing order. Distributed memory parallelism is accomplished through the Message Passing Interface (MPI). All MPI functionality is implemented at the Python level through the `mpi4py` [22] wrapper. Care has been taken to ensure that all requests are persistent and non-blocking. Further, the format of data that is shared between ranks has been made backend independent. PyFR is therefore capable of operation on heterogeneous clusters consisting of both conventional CPUs and accelerators. For reasons of efficiency PyFR introduces its own high-order mesh and solution file formats. A summary of the capabilities of PyFR can be seen in Table 2.

```

1 __global__ void
2 negdivconf(int _ny, int _nx,
3           const fpdtype_t* __restrict__ rcpdjac_v,
4           int ldrcpdjac,
5           fpdtype_t* __restrict__ tdivtconf_v,
6           int ldtdivtconf)
7 {
8     int _x = blockIdx.x*blockDim.x + threadIdx.x;
9
10    for (int _y = 0; _y < _ny && _x < _nx; ++_y)
11    {
12        fpdtype_t rcpdjac, tdivtconf[4];
13
14        // Load rcpdjac
15        rcpdjac = rcpdjac_v[ldrcpdjac*_y + _x];
16
17        // Load tdivtconf
18        tdivtconf[0] = tdivtconf_v[ldtdivtconf*_y + _x + _nx*0];
19        tdivtconf[1] = tdivtconf_v[ldtdivtconf*_y + _x + _nx*1];
20        tdivtconf[2] = tdivtconf_v[ldtdivtconf*_y + _x + _nx*2];
21        tdivtconf[3] = tdivtconf_v[ldtdivtconf*_y + _x + _nx*3];
22
23        tdivtconf[0] *= -rcpdjac;
24        tdivtconf[1] *= -rcpdjac;
25        tdivtconf[2] *= -rcpdjac;
26        tdivtconf[3] *= -rcpdjac;
27
28        // Store tdivtconf
29        tdivtconf_v[ldtdivtconf*_y + _x + _nx*0] = tdivtconf[0];
30        tdivtconf_v[ldtdivtconf*_y + _x + _nx*1] = tdivtconf[1];
31        tdivtconf_v[ldtdivtconf*_y + _x + _nx*2] = tdivtconf[2];
32        tdivtconf_v[ldtdivtconf*_y + _x + _nx*3] = tdivtconf[3];
33    }
34 }

```

Figure 4. Generated CUDA source for the template in Figure 3 for when $N_V = 4$.

```

1 static PYFR_NOINLINE void
2 negdivconf_inner(int _nx,
3                 const fpdtype_t *__restrict__ rcpdjac_v,
4                 fpdtype_t *__restrict__ tdivtconf_v0,
5                 fpdtype_t *__restrict__ tdivtconf_v1,
6                 fpdtype_t *__restrict__ tdivtconf_v2,
7                 fpdtype_t *__restrict__ tdivtconf_v3)
8 {
9     PYFR_ALIGNED(rcpdjac_v);
10    PYFR_ALIGNED(tdivtconf_v0);
11    PYFR_ALIGNED(tdivtconf_v1);
12    PYFR_ALIGNED(tdivtconf_v2);
13    PYFR_ALIGNED(tdivtconf_v3);
14
15    for (int _x = 0; _x < _nx; _x++)
16    {
17        fpdtype_t rcpdjac, tdivtconf[4];
18
19        // Load rcpdjac
20        rcpdjac = rcpdjac_v[_x];
21
22        // Load tdivtconf
23        tdivtconf[0] = tdivtconf_v0[_x];
24        tdivtconf[1] = tdivtconf_v1[_x];
25        tdivtconf[2] = tdivtconf_v2[_x];
26        tdivtconf[3] = tdivtconf_v3[_x];
27
28        tdivtconf[0] *= -rcpdjac;
29        tdivtconf[1] *= -rcpdjac;
30        tdivtconf[2] *= -rcpdjac;
31        tdivtconf[3] *= -rcpdjac;
32
33        // Store tdivtconf
34        tdivtconf_v0[_x] = tdivtconf[0];
35        tdivtconf_v1[_x] = tdivtconf[1];
36        tdivtconf_v2[_x] = tdivtconf[2];
37        tdivtconf_v3[_x] = tdivtconf[3];
38    }
39 }
40
41 void
42 negdivconf(int _ny, int _nx,
43            const fpdtype_t *__restrict__ rcpdjac_v,
44            int lsdrcpdjac,
45            fpdtype_t *__restrict__ tdivtconf_v,
46            int lsdtdivtconf)
47 {
48     #pragma omp parallel for
49     for (int _y = 0; _y < _ny; _y++)
50         negdivconf_inner(_nx, rcpdjac_v + _y*lsdrcpdjac,
51                         tdivtconf_v + (_y*4 + 0)*lsdtdivtconf,
52                         tdivtconf_v + (_y*4 + 1)*lsdtdivtconf,
53                         tdivtconf_v + (_y*4 + 2)*lsdtdivtconf,
54                         tdivtconf_v + (_y*4 + 3)*lsdtdivtconf);
55 }

```

Figure 5. Generated OpenMP annotated C source code for the template in Figure 3 for when $N_V = 4$. The somewhat unconventional structure is necessary to ensure that the kernel is properly vectorised across a range of compilers.

4 Governing Systems

4.1 Euler Equations

The Euler equations govern the flow of an inviscid compressible fluid. They are a time-dependent advection type problem with a non-linear flux function. Expressed in conservative form they read

$$\frac{\partial u}{\partial t} + \nabla \cdot \mathbf{f} = 0, \quad (30)$$

where

$$u = \begin{Bmatrix} \rho \\ \rho v_x \\ \rho v_y \\ \rho v_z \\ E \end{Bmatrix}, \quad \mathbf{f} = \mathbf{f}^{(\text{inv})} = \begin{Bmatrix} \rho v_x & \rho v_y & \rho v_z \\ \rho v_x^2 + p & \rho v_x v_y & \rho v_x v_z \\ \rho v_x v_y & \rho v_y^2 + p & \rho v_y v_z \\ \rho v_x v_z & \rho v_y v_z & \rho v_z^2 + p \\ v_x(E + p) & v_y(E + p) & v_z(E + p) \end{Bmatrix}, \quad (31)$$

in three dimensions. Here ρ is the mass density of the fluid, $\mathbf{v} = (v_x, v_y, v_z)^T$ is the fluid velocity vector, E is the total energy per unit volume and p is the pressure. For a perfect gas the pressure and total energy can be related by the ideal gas law

$$E = \frac{p}{\gamma - 1} + \frac{1}{2}\rho\|\mathbf{v}\|^2, \quad (32)$$

with $\gamma = C_p/C_v$. As the flux does not depend on derivatives of the field variables the Euler equations are an advection type problem. With the fluxes specified all that remains is to prescribe a method for computing common normal fluxes at interfaces. This is often accomplished using an approximate Riemann solver. There exist a variety of such solvers as detailed in [23]. A description of those implemented in PyFR can be found in Appendix A.

4.2 Navier-Stokes Equations

The Navier-Stokes equations can be viewed as an extension of the Euler equations via the inclusion of viscous terms. This results in an advection-diffusion system. Within the framework outlined above the flux now takes the form of $\mathbf{f} = \mathbf{f}^{(\text{inv})} - \mathbf{f}^{(\text{vis})}$ where

$$\mathbf{f}^{(\text{vis})} = \begin{Bmatrix} 0 & 0 & 0 \\ \mathcal{T}_{xx} & \mathcal{T}_{yx} & \mathcal{T}_{zx} \\ \mathcal{T}_{xy} & \mathcal{T}_{yy} & \mathcal{T}_{zy} \\ \mathcal{T}_{xz} & \mathcal{T}_{yz} & \mathcal{T}_{zz} \\ v_i \mathcal{T}_{ix} + \Delta \partial_x T & v_i \mathcal{T}_{iy} + \Delta \partial_y T & v_i \mathcal{T}_{iz} + \Delta \partial_z T \end{Bmatrix}. \quad (33)$$

In the above we have defined $\Delta = \mu C_p / P_r$ where μ is the dynamic viscosity and P_r is the Prandtl number. The components of the stress-energy tensor are given by

$$\mathcal{T}_{ij} = \mu(\partial_i v_j + \partial_j v_i) - \frac{2}{3}\mu\delta_{ij}\nabla \cdot \mathbf{v}. \quad (34)$$

Using the ideal gas law the temperature can be expressed as

$$T = \frac{1}{C_v} \frac{1}{\gamma - 1} \frac{p}{\rho}, \quad (35)$$

with partial derivatives thereof being given according to the quotient rule. Since the Navier-Stokes equations are an advection-diffusion type system it is necessary to both compute a common solution at element boundaries and augment the inviscid Riemann solver to handle the viscous part of the flux. A popular approach is the LDG method as presented in [8, 24]. In this approach the common solution is given $\forall \alpha$ according to

$$\mathfrak{C}(u_L, u_R) = \left(\frac{1}{2} - \beta\right)u_L + \left(\frac{1}{2} + \beta\right)u_R, \quad (36)$$

where β controls the degree of upwinding/downwinding. The common normal interface flux is then prescribed, once again $\forall \alpha$, according to

$$\mathfrak{F}(u_L, u_R, \mathbf{q}_L, \mathbf{q}_R, \hat{\mathbf{n}}_L) = \mathfrak{F}^{(\text{inv})} - \mathfrak{F}^{(\text{vis})}, \quad (37)$$

where $\mathfrak{F}^{(\text{inv})}$ is a suitable inviscid Riemann solver and

$$\mathfrak{F}^{(\text{vis})} = \hat{\mathbf{n}}_L \cdot \left\{ \left(\frac{1}{2} + \beta\right)\mathbf{f}_L^{(\text{vis})} + \left(\frac{1}{2} - \beta\right)\mathbf{f}_R^{(\text{vis})} \right\} + \tau(u_L - u_R), \quad (38)$$

with τ being a penalty parameter, $\mathbf{f}_L^{(\text{vis})} = \mathbf{f}^{(\text{vis})}(u_L, \mathbf{q}_L)$, and $\mathbf{f}_R^{(\text{vis})} = \mathbf{f}^{(\text{vis})}(u_R, \mathbf{q}_R)$. We observe here that if the common solution is upwinded then the common normal flux will be downwinded. Generally, $\beta = \pm 1/2$ as this results in the numerical scheme having a compact stencil and $0 \leq \tau \leq 1$.

4.3 Presentation in Two Dimensions

The above prescriptions of the Euler and Navier-Stokes equations are valid for the case of $N_D = 3$. The two dimensional formulation can be recovered by deleting the fourth rows in the definitions of u , $\mathbf{f}^{(\text{inv})}$ and $\mathbf{f}^{(\text{vis})}$ along with the third columns of $\mathbf{f}^{(\text{inv})}$ and $\mathbf{f}^{(\text{vis})}$. Vectors are now two dimensional with the velocity being given by $\mathbf{v} = (v_x, v_y)^T$.

5 Validation

5.1 Super Accuracy

It is known that under the right circumstances some high order methods can exhibit an order of accuracy greater than $\varphi + 1$. It has been shown in [7] that several FR schemes can exhibit super accuracy. To validate this a square domain $\Omega = [-20, 20]^2$ was decomposed into four structured quad meshes with spacings of $h = 1/3$, $h = 2/7$, $h = 1/4$, and $h = 2/9$. Initial conditions were taken to be those of an isentropic

Euler vortex in a free-stream

$$\rho(\mathbf{x}, t = 0) = \left\{ 1 - \frac{S^2 M^2 (\gamma - 1) \exp 2f}{8\pi^2} \right\}^{\frac{1}{\gamma-1}}, \quad (39)$$

$$\mathbf{v}(\mathbf{x}, t = 0) = \frac{S y \exp f}{2\pi R} \hat{\mathbf{x}} + \left\{ 1 - \frac{S x \exp f}{2\pi R} \right\} \hat{\mathbf{y}}, \quad (40)$$

$$p(\mathbf{x}, t = 0) = \frac{\rho^\gamma}{\gamma M^2}, \quad (41)$$

where $f = (1 - x^2 - y^2)/2R^2$, $S = 13.5$ is the strength of the vortex, $M = 0.4$ is the free-stream Mach number, and $R = 1.5$ is the radius. All meshes were configured with periodic boundary conditions along boundaries of constant x . Along boundaries of constant y the dynamical variables were fixed according to

$$\begin{aligned} \rho(\mathbf{x} = x\hat{\mathbf{x}} \pm 20\hat{\mathbf{y}}, t) &= 1, \\ \mathbf{v}(\mathbf{x} = x\hat{\mathbf{x}} \pm 20\hat{\mathbf{y}}, t) &= \hat{\mathbf{y}}, \\ p(\mathbf{x} = x\hat{\mathbf{x}} \pm 20\hat{\mathbf{y}}, t) &= \frac{1}{\gamma M^2}, \end{aligned}$$

which are simply the limiting values of the initial conditions. Strictly speaking these conditions, on account of the periodicity, result in the modelling of an infinite array of coupled vortices. The impact of this is mitigated by the observation that the exponentially decaying vortex has a characteristic radius which is far smaller than the extent of the domain. Neglecting these effects the analytic solution of the system is a time t is simply a translation of the initial conditions.

Using the analytical solution we can define an L^2 error as

$$\sigma(t)^2 = \int_{-2}^2 \int_{-2}^2 [\rho^\delta(\mathbf{x} + \Delta_y(t)\hat{\mathbf{y}}, t) - \rho(\mathbf{x}, t = 0)]^2 d^2\mathbf{x} \quad (42)$$

where $\rho^\delta(\mathbf{x}, t)$ is the numerical mass density, $\rho(\mathbf{x}, t = 0)$ the analytic mass density, and $\Delta_y(t)$ is the ordinate corresponding to the centre of the vortex at a time t and accounts for the fact that the vortex is translating in a free stream velocity of unity in the y direction. The initial mass density along with the $[-2, -2] \times [2, 2]$ region used to evaluate the error can be seen in Figure 6. At times, t_c , when the vortex is centred on the box the error can be readily computed by integrating over each element inside the box and summing the residuals

$$\sigma(t_c)^2 = \iint [\rho_i^\delta(\tilde{\mathbf{x}}, t_c) - \rho(\mathcal{M}_i(\tilde{\mathbf{x}}), 0)]^2 J_i(\tilde{\mathbf{x}}) d^2\tilde{\mathbf{x}}, \quad (43)$$

where, $\rho_i^\delta(\tilde{\mathbf{x}}, t_c)$ is the approximate mass density inside of the i th element, and $J_i(\tilde{\mathbf{x}})$ the associated Jacobian. These integrals can be approximated by applying Gaussian quadrature

$$\begin{aligned} \sigma(t_c)^2 &\approx J_i(\tilde{\mathbf{x}}_j) [\rho_i^\delta(\tilde{\mathbf{x}}_j, t_c) - \rho(\mathcal{M}_i(\tilde{\mathbf{x}}_j), 0)]^2 \omega_j \\ &= \frac{h^2}{4} [\rho_i^\delta(\tilde{\mathbf{x}}_j, t_c) - \rho(\mathcal{M}_i(\tilde{\mathbf{x}}_j), 0)]^2 \omega_j, \end{aligned} \quad (44)$$

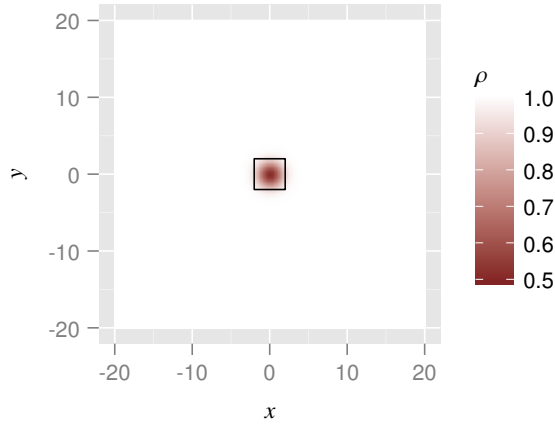


Figure 6. Initial density profile for the vortex in Ω . The black box shows the region where the error is calculated.

where $\{\tilde{x}_j\}$ are abscissa and $\{\omega_j\}$ the weights of a rule determined for integration inside of a standard quad. So long as the rule used is of adequate strength then this will be a very good approximation of the true L^2 error.

Following [25] the initial conditions were laid onto the mesh using a collocation projection with $\varphi = 3$. The simulation was then run with the DG, SD, and HU schemes. Solution points were placed at a tensor product construction of Gauss-Legendre quadrature points. Common interface fluxes were computed using a Rusanov Riemann solver. To advance the solutions in time a classical fourth order Runge-Kutta method (RK4) was used. The time step was taken to be $\Delta t = 0.00125$ with $t = 0..1800$ with solutions written out to disk every 32 000 steps. The order of accuracy of the scheme at a particular time can be determined by plotting $\log \sigma$ against $\log h$ and performing a least-squares fit through the four data points. The order is given by the gradient of the fit. A plot of order of accuracy against time for the three schemes can be seen in Figure 7. We note that the order of accuracy changes as a function of time. This is due to the fact that the error is actually of the form $\sigma(t) = \sigma_p + \sigma_{so}(t)$ where σ_p is a constant projection error and σ_{so} is a time-dependent spatial operator error. The projection error arises as a consequence of the fourth order collocation projection of the initial conditions onto the mesh. Over time the spatial operator error grows in magnitude and eventually dominates. Only when $\sigma_{so}(t) \gg \sigma_p$ can the true order of the method be observed. The results here can be seen to be in excellent agreement with those of [25].

5.2 Couette Flow

Consider the case in which two parallel plates of infinite extent are separated by a distance H in the y direction. We treat both plates as isothermal walls at a temperature T_w and permit the top plate to move at a velocity v_w in the x direction with respect to the bottom plate. For simplicity we shall take the ordinate of

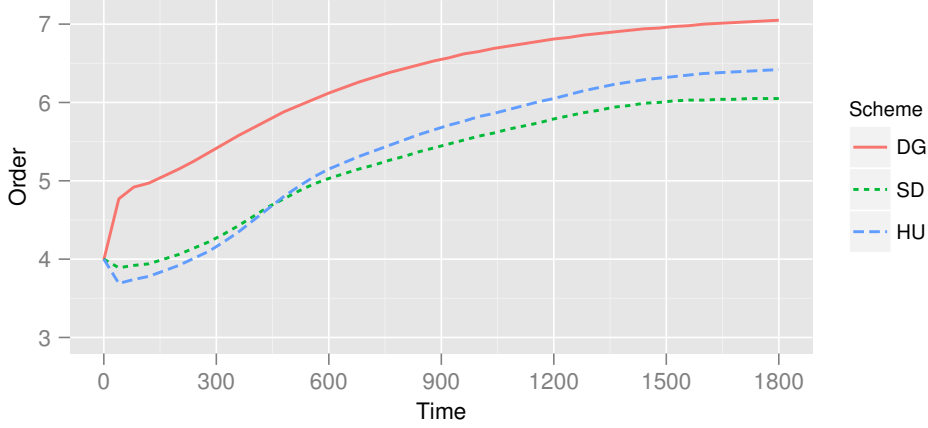


Figure 7. Spatial super accuracy observed for a $\phi = 3$ simulation.

the bottom plate as zero. In the case of a constant viscosity μ the Navier-Stokes equations admit an analytical solution in which

$$\rho(\phi) = \frac{\gamma}{\gamma - 1} \frac{2p}{2C_p T_w + P_r v_w^2 \phi(1 - \phi)}, \quad (45)$$

$$\mathbf{v}(\phi) = v_w \phi \hat{\mathbf{x}}, \quad (46)$$

$$p = p_c, \quad (47)$$

where $\phi = y/H$ and p_c is a constant pressure. The total energy is given by the ideal gas law of Equation 32. On a finite domain the Couette flow problem can be modelled through the imposition of periodic boundary conditions. For a two dimensional mesh periodicity is enforced in x whereas for three dimensional meshes it is enforced in both x and z . To validate the Navier-Stokes solver in PyFR we take $\gamma = 1.4$, $P_r = 0.72$, $\mu = 0.417$, $C_p = 1005 \text{ J K}^{-1}$, $H = 1 \text{ m}$, $T_w = 300 \text{ K}$, $p_c = 1 \times 10^5 \text{ Pa}$, and $v_w = 69.445 \text{ m s}^{-1}$. These values correspond to a Mach number of 0.2 and a Reynolds number of 200. The plates were modelled as no-slip isothermal walls as detailed in subsection B.3 of Appendix B. A plot of the resulting energy profile can be seen in Figure 8. Constant initial conditions are taken as $\rho = \langle \rho(\phi) \rangle$, $\mathbf{v} = v_w \hat{\mathbf{x}}$, and $p = p_c$. Using the analytical solution we again define an L^2 error as

$$\sigma(t)^2 = \iint_{\Omega} [E^\delta(\mathbf{x}, t) - E(\mathbf{x})]^2 d^2 \mathbf{x} \quad (48)$$

$$= \iint_{\Omega_{ei}} [E_{ei}^\delta(\tilde{\mathbf{x}}, t) - E(\mathcal{M}_{ei}(\tilde{\mathbf{x}}))]^2 J_{ei}(\tilde{\mathbf{x}}) d^2 \tilde{\mathbf{x}} \quad (49)$$

$$\approx [E_{ei}^\delta(\tilde{\mathbf{x}}_{ej}, t) - E(\mathcal{M}_{ei}(\tilde{\mathbf{x}}_{ej}))]^2 J_{ei}(\tilde{\mathbf{x}}_{ej}) \omega_{ej} \quad (50)$$

where Ω is the computational domain, $E^\delta(\mathbf{x}, t)$ is the numerical total energy, and $E(\mathbf{x})$ the analytic total energy. In the third step we have approximated each integral

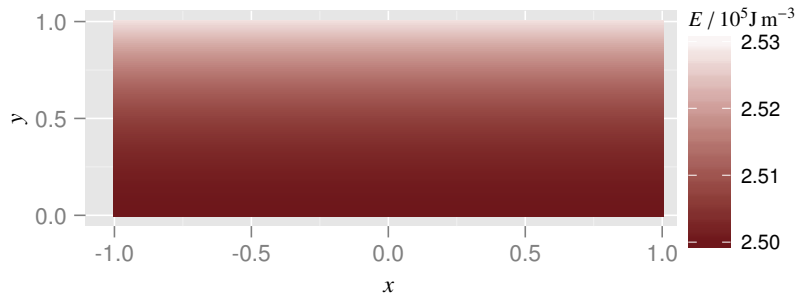


Figure 8. Converged steady state energy profile for the two dimensional Couette flow problem.

by a Gaussian quadrature rule with abscissa $\{\tilde{\mathbf{x}}_{e_j}\}$ and weights $\{\omega_{e_j}\}$ inside of an element type e . Couette flow is a steady state problem and so in the limit of $t \rightarrow \infty$ the numerical total energy should converge to a solution. Hence, when starting from constant initial conditions we need to march forward in time until the residual is zero to within machine precision. Once the system has converged for a range of meshes it is possible to compute the order of accuracy of the scheme. For a given φ this is the slope (plus or minus a standard error) of a linear least squares fit of $\log h \sim \log \sigma(t_\infty)$ where h is an approximation of the characteristic grid spacing. The expected order of accuracy is $\varphi + 1$. In all simulations inviscid fluxes were computed using the Rusanov approach and the LDG parameters were taken to be $\beta = 1/2$ and $\tau = 0.1$. All simulations were performed with DG correction functions and at double precision. Inside tensor product elements Gauss-Legendre solution and flux points were employed. Triangular elements utilised Williams-Shunn solution points and Gauss-Legendre flux points.

Two dimensional unstructured mixed mesh. For the two dimensional test cases the computational domain was taken to be $[-1, 1] \times [0, 1]$. This domain was then meshed with both triangles and quadrilaterals at four different refinement levels. The Couette flow problem described above was then solved on each of these meshes. Experimental L^2 errors and orders of accuracy can be seen in Table 3. We note that in all cases the expected order of accuracy was obtained.

Three dimensional extruded hexahedral mesh. For this three dimensional case the computational domain was taken to be $[-1, 1] \times [0, 1] \times [0, 1]$. Meshes were constructed through first generating a series of unstructured quadrilateral meshes in the x - y plane. A three layer extrusion was then performed on this meshes to yield a series of hexahedral meshes. Experimental L^2 errors and orders of accuracy for these meshes can be seen in Table 4.

Three dimensional unstructured hexahedral mesh. As a further test a domain of dimension $[0, 1]^3$ was considered. This domain was meshed using completely

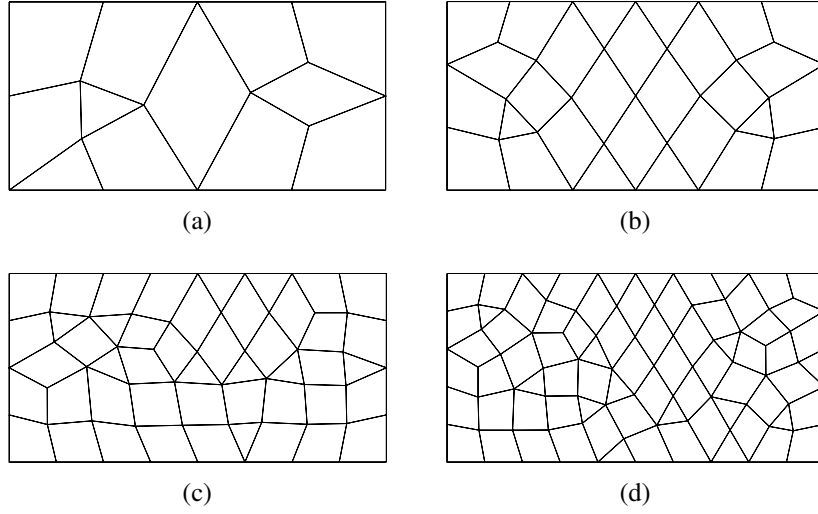


Figure 9. Unstructured mixed element meshes used for the two dimensional Couette flow problem.

Table 3. L^2 energy error and orders of accuracy for the Couette flow problem on four mixed meshes. The mesh spacing was approximated as $h \sim N_E^{-1/2}$ where N_E is the total number of elements in the mesh.

Tris	Quads	$\sigma(t_\infty) / \text{J m}^{-3}$			
		$\varphi = 1$	$\varphi = 2$	$\varphi = 3$	$\varphi = 4$
2	8	1.26×10^2	5.77×10^{-1}	5.54×10^{-3}	6.62×10^{-5}
6	22	3.56×10^1	1.40×10^{-1}	6.72×10^{-4}	3.91×10^{-6}
10	37	2.08×10^1	4.35×10^{-2}	2.54×10^{-4}	8.16×10^{-7}
16	56	1.46×10^1	3.52×10^{-2}	1.09×10^{-4}	4.62×10^{-7}
Order		2.21 ± 0.12	2.99 ± 0.32	3.97 ± 0.05	5.20 ± 0.38

Table 4. L^2 energy errors and orders of accuracy for the Couette flow problem on three extruded hexahedral meshes. On account of the extrusion $h \sim N_E^{-1/2}$ where N_E is the total number of elements in the mesh.

Hexes	$\sigma(t_\infty) / \text{J m}^{-3}$		
	$\varphi = 1$	$\varphi = 2$	$\varphi = 3$
78	3.35×10^1	5.91×10^{-2}	7.28×10^{-4}
195	1.23×10^1	1.87×10^{-2}	1.15×10^{-4}
405	6.15×10^0	5.49×10^{-3}	2.72×10^{-5}
Order	2.06 ± 0.08	2.87 ± 0.24	3.99 ± 0.03

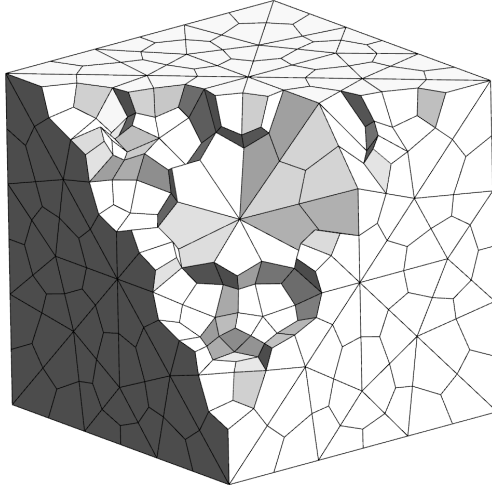


Figure 10. Cutaway of the unstructured hexahedral mesh with 1004 elements.

Table 5. L^2 energy errors and orders of accuracy for the Couette flow problem on three unstructured hexahedral meshes. Mesh spacing was taken as $h \sim N_E^{-1/3}$ where N_E is the total number of elements in the mesh.

Hexes	$\sigma(t_\infty) / \text{J m}^{-3}$		
	$\wp = 1$	$\wp = 2$	$\wp = 3$
96	1.91×10^1	4.32×10^{-2}	5.83×10^{-4}
536	8.20×10^0	9.11×10^{-3}	6.89×10^{-5}
1004	3.82×10^0	3.22×10^{-3}	2.04×10^{-5}
Order	1.93 ± 0.46	3.19 ± 0.48	4.16 ± 0.44

unstructured hexahedra. Three levels of refinement were used resulting in meshes with 96, 536 and 1004 elements. A cutaway of the most refined mesh can be seen in Figure 10. Experimental L^2 errors and the resulting orders of accuracy are presented in Table 5. Despite the fully unstructured nature of the mesh a suitable order of accuracy was again obtained in all cases. We do, however, note the higher standard errors associated with these results.

5.3 Flow Over a Cylinder

In order to demonstrate the ability of PyFR to solve unsteady problems the flow over a cylinder at Reynolds number 3600 and Mach number $M = 0.2$ was investigated. A cylinder of radius $1/2$ was placed at $(0, 0)$ inside of a domain of dimension $[-18, 30] \times [-10, 10] \times [0, 3.2]$. This domain was then meshed in the x - y plane with 4661 quadratically curved quadrilateral elements. Next, this grid was extruded along the z -axis to yield a total of 46610 hexahedra. The grid, which can be seen in

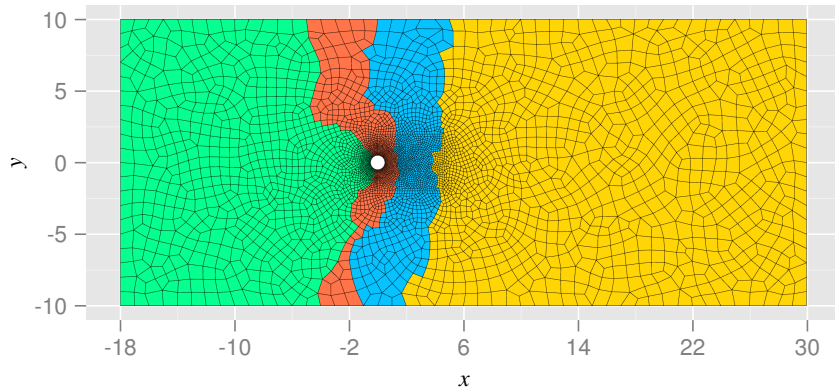


Figure 11. Cross section in the x - y plane of the cylinder mesh. Colours indicate the partition to which the elements belong.

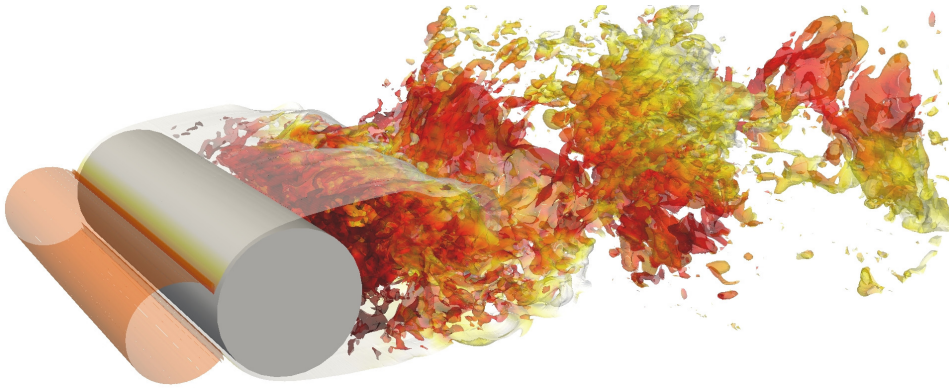


Figure 12. Isosurfaces of density around the cylinder.

Figure 11, was partitioned into four pieces. Along surfaces of $y = \pm 10$ and $x = -18$ the inflow boundary condition of subsection B.1 in Appendix B was imposed. Along the surface of $x = 30$ the outflow condition of subsection B.2 in Appendix B was used. Periodic conditions were imposed in the z direction. On the surface of the cylinder the no-slip isothermal wall condition of subsection B.3 in Appendix B was imposed. The free-stream conditions were taken to be $\rho = 1$, $\mathbf{v} = \hat{\mathbf{x}}$, and $p = 1/\gamma M^2$. These were also used as the initial conditions for the simulation. DG correction functions were used with the LDG parameters being $\beta = 1/2$ and $\tau = 0.1$. The ratio of specific heats was taken as $\gamma = 1.4$ and the Prandtl number as $P_r = 0.72$.

The simulation was run with $\varphi = 4$ with four NVIDIA K20c GPUs. It contained some 29×10^6 degrees of freedom. Isosurfaces of density captured after the turbulent wake had fully developed can be seen in Figure 12.

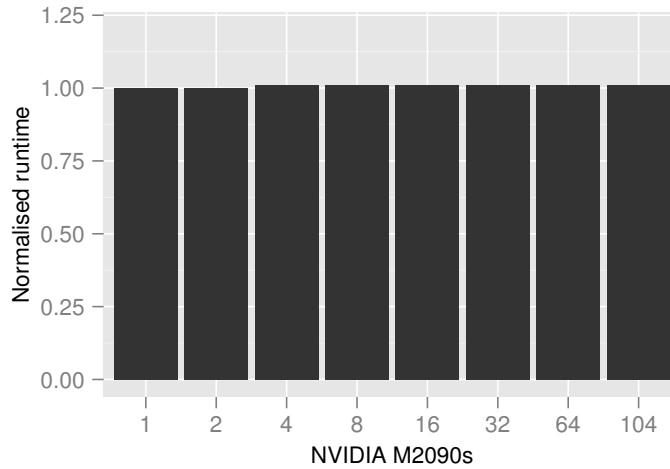


Figure 13. Weak scalability of PyFR for the Navier-Stokes equations with $\varphi = 3$.

6 Scalability

The scalability of PyFR has been evaluated on the Emerald GPU cluster. It is housed at the STFC Rutherford Appleton Laboratory and based around 60 HP SL390 nodes with three NVIDIA M2090 GPUs and 24 HP SL390 nodes with eight NVIDIA M2090 GPUs. Nodes are connected by QDR InfiniBand. For simplicity all runs herein were performed on the eight GPU nodes. As a starting point a domain of dimension $[-16, 16] \times [-16, 16] \times [0, 1.75]$ was meshed isotropically with $N_E = 114688$ structured hexahedral elements. The mesh was configured with completely periodic boundary conditions. When run with the Navier-Stokes solver in PyFR with $\varphi = 3$ the mesh gives a working set of ~ 4720 MiB. This is sufficient to 90% load an M2090 which when ECC is enabled has ~ 5250 MiB memory available to the user. When examining the scalability of a code there are two commonly used metrics. The first of these is weak scalability in which the size of the target problem is increased in proportion to the number of ranks N with $N_E \propto N$. For a code with perfect weak scalability the runtime should remain unchanged as more ranks are added. The second metric is strong scalability wherein the problem size is fixed and the speedup compared to a single rank is assessed. Perfect strong scalability implies that the runtime scales as $1/N$.

For the domain outlined above weak scalability was evaluated by increasing the dimensions of the domain according to $[-16, 16] \times N[-16, 16] \times [0, 1.75]$. This extension permitted the domain to be trivially decomposed along the y -axis. The resulting runtimes for $1 \leq N \leq 104$ can be seen in Figure 13. We note that in the $N = 104$ case that the simulation consisted of some 3.8×10^9 degrees of freedom with a working set of ~ 485 GiB.

To study the strong scalability the initial domain was partitioned along the x - and y -axes. Each partition contained exactly N_E/Ns . The resulting speedups for $1 \leq N \leq 32$ can be seen in Figure 14. Up to eight GPUs scalability can be seen to

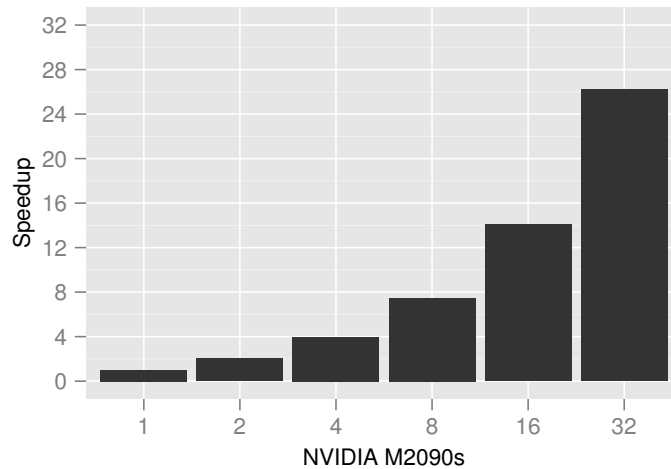


Figure 14. Strong scalability of PyFR for the Navier-Stokes equations with $\varphi = 3$ showing the speedup relative to a single GPU.

be near perfect. Beyond this the relationship begins to break down. When $N = 32$ an improvement of 26 can be observed. However, in this case each GPU is loaded to less than 3% and so the result is to be expected.

7 Conclusions

In this paper we have described PyFR, an open source Python framework for solving advection-diffusion type problems on streaming architectures. The structure and ethos of PyFR has been explained including our methodology for targeting multiple hardware platforms. Further, a case has been made for the use of a high-level scripting language within the context of an HPC code. We have shown that PyFR exhibits spatial super accuracy when solving the 2D Euler equations and the expected order of accuracy when solving Couette flow problem on a range of grids in 2D and 3D. Qualitative results for unsteady 3D viscous flow problems on curved grids have also been presented. The scalability of PyFR has been demonstrated in the strong sense up to 32 NVIDIA M2090s and in the weak sense up to 104 NVIDIA M2090s when solving the 3D Navier-Stokes equations.

Acknowledgements

The authors would like to thank the Engineering and Physical Sciences Research Council for their support via two Doctoral Training Grants and an Early Career Fellowship (EP/K027379/1). The authors would also like to thank the e-Infrastructure South Centre for Innovation for granting access to the Emerald supercomputer, and NVIDIA for donation of three K20c GPUs.

A Riemann Solvers

In the following section we take u_L and u_R to be the two discontinuous solution states at an interface and $\hat{\mathbf{n}}_L$ to be the normal vector associated with the first state. For convenience we take $\mathbf{f}_L^{(\text{inv})} = \mathbf{f}^{(\text{inv})}(u_L)$, and $\mathbf{f}_R^{(\text{inv})} = \mathbf{f}^{(\text{inv})}(u_R)$ with inviscid fluxes being prescribed by Equation 31.

A.1 Rusanov

Also known as the local Lax-Friedrichs method a Rusanov type Riemann solver imposes inviscid numerical interface fluxes according to

$$\mathfrak{F}^{(\text{inv})} = \frac{\hat{\mathbf{n}}_L}{2} \cdot \{\mathbf{f}_L^{(\text{inv})} + \mathbf{f}_R^{(\text{inv})}\} + \frac{s}{2}(u_L - u_R), \quad (51)$$

where s is an estimate of the maximum wave speed

$$s = \sqrt{\frac{\gamma(p_L + p_R)}{\rho_L + \rho_R}} + \frac{1}{2}|\hat{\mathbf{n}}_L \cdot (\mathbf{v}_L + \mathbf{v}_R)|. \quad (52)$$

B Boundary Conditions

B.1 Supersonic Inflow

The supersonic inflow condition is parameterised by a free-stream density ρ_f , velocity \mathbf{v}_f , and pressure p_f .

$$\mathcal{B}^{(\text{inv})} u_L = \mathcal{B}^{(\text{ldg})} u_L = \begin{cases} \rho_f \\ \rho_f \mathbf{v}_f \\ p_f / (\gamma - 1) + \frac{\rho_f}{2} \|\mathbf{v}_f\|^2 \end{cases}, \quad (53)$$

$$\mathcal{B}^{(\text{ldg})} \mathbf{q}_L = 0, \quad (54)$$

B.2 Subsonic Outflow

Subsonic outflow boundaries are parameterised by a free-stream pressure p_f .

$$\mathcal{B}^{(\text{inv})} u_L = \mathcal{B}^{(\text{ldg})} u_L = \begin{cases} \rho_L \\ \rho_L \mathbf{v}_L \\ p_f / (\gamma - 1) + \frac{\rho_L}{2} \|\mathbf{v}_L\|^2 \end{cases}, \quad (55)$$

$$\mathcal{B}^{(\text{ldg})} \mathbf{q}_L = 0, \quad (56)$$

B.3 No-slip Isothermal Wall

The no-slip isothermal wall condition depends on the wall temperature $C_p T_w$ and the wall velocity \mathbf{v}_w . Usually $\mathbf{v}_w = 0$.

$$\mathcal{B}^{(\text{inv})} u_L = \rho_L \left\{ \begin{array}{c} 1 \\ 2\mathbf{v}_w - \mathbf{v}_L \\ C_p T_w / \gamma + \frac{1}{2} \|\mathbf{v}_w - \mathbf{v}_L\|^2 \end{array} \right\}, \quad (57)$$

$$\mathcal{B}^{(\text{ldg})} u_L = \rho_L \left\{ \begin{array}{c} 1 \\ \mathbf{v}_w \\ C_p T_w / \gamma + \frac{1}{2} \|\mathbf{v}_w\|^2 \end{array} \right\}, \quad (58)$$

$$\mathcal{B}^{(\text{ldg})} \mathbf{q}_L = \mathbf{q}_L, \quad (59)$$

References

- [1] PE Vincent and A Jameson. Facilitating the adoption of unstructured high-order methods amongst a wider community of fluid dynamicists. *Mathematical Modelling of Natural Phenomena*, 6(03):97–140, 2011.
- [2] TJ Barth and PO Frederickson. Higher order solution of the Euler equations on unstructured grids using quadratic reconstruction. *AIAA paper 90-0013*, 1990.
- [3] Xu-Dong Liu, Stanley Osher, and Tony Chan. Weighted essentially non-oscillatory schemes. *Journal of computational physics*, 115(1):200–212, 1994.
- [4] WH Reed and TR Hill. Triangular mesh methods for the neutron transport equation. *Technical Report LA-UR-73-479, Los Alamos Scientific Laboratory*, 1973.
- [5] David A Kopriva and John H Koliass. A conservative staggered-grid Chebyshev multidomain method for compressible flows. *Journal of computational physics*, 125(1):244–261, 1996.
- [6] Yuzhi Sun, Zhi Jian Wang, and Yen Liu. High-order multidomain spectral difference method for the Navier-Stokes equations on unstructured hexahedral grids. *Communications in Computational Physics*, 2(2):310–333, 2007.
- [7] HT Huynh. A flux reconstruction approach to high-order schemes including discontinuous Galerkin methods. *AIAA paper*, 4079:2007, 2007.
- [8] Jan S Hesthaven and Tim Warburton. *Nodal discontinuous Galerkin methods: algorithms, analysis, and applications*, volume 54. Springer Verlag New York, 2008.

- [9] David A Kopriva. A staggered-grid multidomain spectral method for the compressible navier–stokes equations. *Journal of Computational Physics*, 143(1):125–158, 1998.
- [10] PE Vincent, P Castonguay, and A Jameson. A new class of high-order energy stable flux reconstruction schemes. *Journal of Scientific Computing*, 47(1):50–72, 2011.
- [11] A Jameson, PE Vincent, and P Castonguay. On the non-linear stability of flux reconstruction schemes. *Journal of Scientific Computing*, 50(2):434–445, 2011.
- [12] DM Williams. *Energy Stable High-Order Methods for Simulating Unsteady, Viscous, Compressible Flows on Unstructured Grids*. PhD thesis, Stanford University, Jun 2013.
- [13] P Castonguay, PE Vincent, and A Jameson. A new class of high-order energy stable flux reconstruction schemes for triangular elements. *Journal of Scientific Computing*, 2011.
- [14] FD Witherden and PE Vincent. An analysis of solution point coordinates for flux reconstruction schemes on triangular elements. *Submitted for publication in Journal of Scientific Computing*, 2013.
- [15] D.M. Williams and A. Jameson. Energy stable flux reconstruction schemes for advection–diffusion problems on tetrahedra. *Journal of Scientific Computing*, pages 1–39, 2013.
- [16] D Williams and A Jameson. Nodal points and the nonlinear stability of high-order methods for unsteady flow problems on tetrahedral meshes. In *43rd AIAA Fluid Dynamics Conference*, 2013.
- [17] Lee Shunn and Frank Ham. Symmetric quadrature rules for tetrahedra based on a cubic close-packed lattice arrangement. *Journal of Computational and Applied Mathematics*, 236(17):4348–4364, 2012.
- [18] Patrice Castonguay, David M Williams, Peter E Vincent, Manuel Lopez, and Antony Jameson. On the development of a high-order, multi-gpu enabled, compressible viscous flow solver for mixed unstructured grids. *AIAA paper*, 3229:2011, 2011.
- [19] SymPy Development Team. SymPy: Python library for symbolic mathematics, 2013.
- [20] Andreas Klöckner, Nicolas Pinto, Yunsup Lee, Bryan Catanzaro, Paul Ivanov, and Ahmed Fasih. Pycuda and pyopencl: A scripting-based approach to gpu run-time code generation. *Parallel Comput.*, 38(3):157–174, 2012.

- [21] Michael Bayer. Mako: Templates for python, 2013.
- [22] Lisandro Dalcin. mpi4py: Mpi for python, 2013.
- [23] Eleuterio F Toro. *Riemann solvers and numerical methods for fluid dynamics: a practical introduction*. Springer, 2009.
- [24] P Castonguay, DM Williams, PE Vincent, and A Jameson. Energy stable flux reconstruction schemes for advection-diffusion problems. *Computer Methods in Applied Mechanics and Engineering*, 2013.
- [25] PE Vincent, P Castonguay, and A Jameson. Insights from von Neumann analysis of high-order flux reconstruction schemes. *Journal of Computational Physics*, 230(22):8134–8154, 2011.